



Regulating donor-acceptor interactions in triazine-based conjugated polymers for boosted photocatalytic hydrogen production

Zhaolin Li^a, Hua Fang^a, Zupeng Chen^a, Weixin Zou^b, Chengxiao Zhao^{a,*}, Xiaofei Yang^{a,*}

^a Jiangsu Co-Innovation Center of Efficient Processing and Utilization of Forest Resources, International Innovation Center for Forest Chemicals and Materials, College of Science, Nanjing Forestry University, Nanjing 210037, PR China

^b Jiangsu Key Laboratory of Vehicle Emissions Control, Center of Modern Analysis, Nanjing University, Nanjing 210093, PR China

ARTICLE INFO

Keywords:

Photocatalysis
Hydrogen evolution reaction
Triazine
Conjugated polymer
Donor-acceptor interaction

ABSTRACT

The donor-acceptor (D-A) interactions between the triazine ring unit and adjacent substituents is one of the decisive factors that affect the performance of triazine-based conjugated polymer photocatalysts. Herein, we design and synthesize novel conjugated polymers by introducing electron-drawing 1,3,4-oxadiazole units into 1,3,5-triazine-based π -conjugated skeletons for photocatalytic hydrogen production. Compared with the bulk polymer, the modified photocatalysts show extended visible light harvesting and boosted charge separation. Notably, under the irradiation of full-spectrum solar light, as-synthesized polymer with bi-1,3,4-oxadiazole linkage (denoted as TCP-BOXD) shows a highly improved hydrogen-evolving rate up to $3000 \mu\text{mol g}^{-1} \text{h}^{-1}$. Furthermore, DFT calculation reveals that N atoms in the introduced 1,3,4-oxadiazole unit, coupled with those in the triazine ring, act as synergistic bi-active sites for superior photocatalytic hydrogen production. Our findings may help the rational design and controllable synthesis of novel triazine-based conjugated polymers for photocatalysis.

1. Introduction

The last decades have witnessed remarkable advancements and the development in high-efficient photocatalytic materials for energy and environmental applications [1–15]. Since the discovery of oligo-/poly (*p*-phenylene)s for photocatalytic hydrogen evolution in 1985 [16], conjugated polymer semiconductor photocatalysts have aroused tremendous research interest due to their tunable structure and outstanding photo-/thermostability. Excellent polymer photocatalysts have common features that are large π -delocalization and suitable electronic structures [17,18]. For instance, the planar pyrene unit is usually integrated with conjugated linkages to enhance the electron delocalization of skeletons [19–21]. In another case of heptazine-based carbon nitrides, the heptazine oligomer shows a large π -conjugation and high electron affinity which drives the proton reduction in thermodynamics [22,23]. However, the majority of polymer semiconductors typically suffer from large exciton binding energy and low electron/hole migration, especially the ones consisting of a single building block, which cause high rates of excitation recombination. To relieve this limitation, the electron donor-acceptor (D-A) dyads are further designed and incorporated into the conjugated polymer skeletons to facilitate free

photogenerated charge carriers escaping to the surface of materials. Because the D-A conjugated dyads cannot only promote π -delocalization but also form a regional polarization which can accelerate the electron migration [24,25].

The covalent triazine frameworks (CTFs) are one of well-known D-A type conjugated polymer photocatalysts, in which the electron-withdrawing *s*-triazine unit not only suppress photogenerated charge recombination but also can produce extraordinary heteroatom effects and active sites [26–28]. Especially, CTF-1 constructed alternately from 1,3,5-triazine unit (electron acceptor) and phenylene (electron donor) has been investigated extensively on photocatalytic hydrogen production [17,27]. Researchers focus on developing synthetic methods to improve the crystallinity of CTF-1, which can effectively tune the electronic structure and facilitate electron transfer between adjacent layers [29,30]. However, this approach offers limited improvement on charge carrier separation and migration for CTF-1, resulting in unsatisfied hydrogen evolution reaction performance. Alternative promising strategy to improve photocatalytic performance has been raised, i.e. reconstruct and optimize the D-A dyad structure. A variety of electron-withdrawing building blocks, such as aromatic units [31], aromatic heterocyclic units [24,32], benzoheterocyclic units [33–35],

* Corresponding authors.

E-mail addresses: chengxiaozhao@njfu.edu.cn (C. Zhao), xiaofei.yang@njfu.edu.cn (X. Yang).

<https://doi.org/10.1016/j.apcatb.2022.121374>

Received 30 January 2022; Received in revised form 20 March 2022; Accepted 2 April 2022

Available online 4 April 2022

0926-3373/© 2022 Elsevier B.V. All rights reserved.

unsaturated bonds [36–38] were incorporated into the skeletons and frameworks to form new D-A structures and D- π -A structures. It has been documented that benzotrithiophene and naphthodithiophene as excellent electron-donating blocks can form strong D-A interaction by directly bonding with 1,3,5-triazine, which enables strong charge-transfer effects [39]. However, it is worth noting that over-strong D-A interactions can facilitate charge carrier migration and separation, but unavoidably widen the bandgaps [39,40]. Furthermore, the introduction of an extended π -conjugated linkage can enlarge delocalization, whereas it may also prolong the charge carrier migration distance or skeleton torsion, thus hindering efficient electron-hole separation. Moreover, D- π -A structure can further promote charges transfer and separation, due to that the π -spacer can reduce backward charge recombination, minimize exciton binding energy and increase charge carrier lifetime [41]. However, except for acetylene groups, there are few suitable conjugated units as bridged π -spacer [38].

Here, we report a novel triazine-based conjugated polymer photocatalyst synthesized by introducing an electron-drawing unit into the D-A structures to moderate the D-A interactions and suppress the electron-hole recombination. Given the heterocyclic 1,3,4-oxadiazole unit exhibits remarkable intramolecular charge transfer when linked with phenyls [42,43], 1,3,4-oxadiazole as an electron-drawing unit is incorporated into the skeletons of CTFs for the first time. Both experimental evidences and density functional theory (DFT) calculations reveal that 1,3,4-oxadiazole units in novel 1,3,5-triazine-based conjugated polymer photocatalysts act as π -spacers to enhance the co-planarity and the π -delocalization, and N atoms in 1,3,4-oxadiazole act as synergistic bi-active sites. The modified framework is beneficial for the efficient separation of photogenerated charge carriers and subsequently, for superior photocatalytic hydrogen production from water splitting. Notably, the electron-drawing nature of 1,3,4-oxadiazole affects the D-A interaction between 1,3,5-triazine and phenylene, which also endows the modified polymer photocatalyst with enhanced wide-spectrum visible light harvesting. This study proposes that introducing suitable conjugated heterocycles into the skeleton of D-A type conjugated polymers is a feasible strategy for designing high-performance photocatalysts.

2. Experimental section

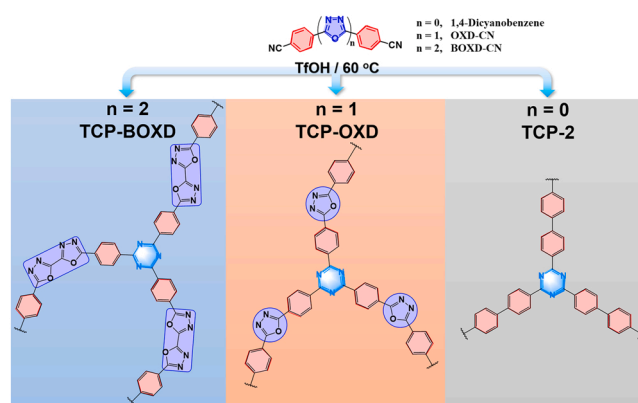
2.1. Chemicals and materials

Methyl 4-cyanobenzoate, 4-cyanobenzoyl chloride, trifluoromethanesulfonic acid (TfOH), oxalyl chloride, and ammonia were purchased from Aladdin. Tetrahydrofuran (THF), *p*-dioxane, *N*-Methyl-2-Pyrrolidone (NMP), dimethyl sulfoxide (DMSO), acetone, ethanol, acetonitrile, thionyl chloride, and hydrazine hydrate (85%) were from Sinopharm Chemical Reagent Co., Ltd.

2.2. Synthesis of catalysts

Conjugated precursors containing 1,3,4-oxadiazole units were synthesized by a modified method according to the literature [44] (Scheme S1, Figs. S1–S10). New triazine-based conjugated polymers with 1,3,4-oxadiazole linkages were synthesized from corresponding precursors via trimerization reactions catalyzed by trifluoromethanesulfonic acid (TfOH) as shown in Scheme 1.

Typically, a certain amount of monomers (OXD-CN, 500 mg; BOXD-CN 420 mg; and 4,4'-dicyanobiphenyl, 120 mg) was dissolved in 6 mL of TfOH at -10°C . Then, the reaction mixture was stirring at -10°C , room temperature and 70°C for 20 min, 3 h and 40 min, respectively. Finally, poured the mixture into 200 mL of ice-water and neutralized the solution with ammonia. The obtained solid was filtered out, washed with deionized water and ethanol, and followed by soxhlet extraction with deionized water, ethanol and acetone. The solid was grounded into powder for following measurements. The final samples obtained by



Scheme 1. Synthetic routes of TCP-2, TCP-OXD and TCP-BOXD.

polymerization of OXD-CN, BOXD-CN and 4,4'-dicyanobiphenyl were denoted as TCP-OXD, TCP-BOXD and TCP-2, respectively.

2.3. Material characterization

Precursors and skeletons of conjugated polymers were verified by the Fourier transform infrared (FT-IR) spectroscopy (Nicolet Model Nexus 470), ^{13}C cross-polarization magic-angle-spinning (CP-MAS) solid-state nuclear magnetic resonance (NMR) spectroscopy (AVANCE NEO), and X-ray photoelectron spectroscopy (XPS, Perkin-Elmer PHI 500). The crystal structures and morphologies of samples were characterized by X-ray diffraction (XRD, Ultima IV) and cold field emission scanning electron microscope (SEM, Regulus 8100), respectively. UV–visible diffuse reflection spectroscopy (DRS) and electron paramagnetic resonance (EPR) measurements were recorded on Lambda 950 spectrometer and JES FA 200 spectrometer, respectively. Electron spin resonance (ESR) signal were detected on Bruker model A300 spectrometer, using 5, 5-dimethyl-1-pyrroline N-oxide (DMPO) as the photogenerated radical (i. e. $\bullet\text{OH}$, $\bullet\text{O}_2^-$) spin-trapping reagents. SPV response measurements were conducted by a system equipped with a third-harmonic Nd:YAG laser (Polaris II, New Wave Research, Inc.) and a 500 MHz digital phosphor oscilloscope (TDS 5054, Tektronix).

Femtosecond pump-probe transient absorption spectroscopy (TAS) measurements were performed using a regenerative amplified Ti:Sapphire laser system (Coherent; 800 nm, 70 fs, 6 mJ/pulse, and 1 kHz repetition rate) as the laser source and a femto-TA100 spectrometer (Time-Tech Spectra) [45]. Typically, the 800 nm output pulse from the regenerative amplifier was split in two parts with a 50% beam splitter. The transmitted part was used to pump a TOPAS Optical Parametric Amplifier (OPA) which generates a wavelength-tunable laser pulse from 250 nm to $2.5\ \mu\text{m}$ as pump beam. The reflected 800 nm beam was split again into two parts. One part with less than 10% was attenuated with a neutral density filter and focused into a 2 mm thick sapphire window to generate a white light continuum (WLC) used for probe beam. The probe beam was focused with an Al parabolic reflector onto the sample. After the sample, the probe beam was collimated and then focused into a fiber-coupled spectrometer with CMOS sensors and detected at a frequency of 1 KHz. The intensity of the pump pulse used in the experiment was controlled by a variable neutral-density filter wheel. The delay between the pump and probe pulses was controlled by a motorized delay stage. The pump pulses were chopped by a synchronized chopper at 500 Hz and the absorbance change was calculated with two adjacent probe pulses (pump-blocked and pump-unblocked). The samples were placed in 1 mm airtight cuvettes in a N_2 -filled glove box and measured under ambient conditions. Samples were vigorously stirred in all the measurements.

2.4. Electrochemical measurements

Photocurrent-time (I-t) plots, electrochemical impedance spectra (EIS), and Mott-Schottky plots were recorded on a CHI-760E electrochemical workstation (Shanghai Chenhua) with a standard three-electrode system. The catalyst-coated fluorine-doped tin oxide glass (FTO), Pt plate, and Ag/AgCl electrodes served as the working electrode, counter electrode and reference electrode, respectively. These measurements were performed in the electrolyte of 0.2 M Na₂SO₄ solution (pH = 6.8). A LED lamp (50 W) was used as light source during the measurement. The applied potentials vs. Ag/AgCl is converted to RHE potentials using Eq. (1), $E_{\text{AgCl}} = 0.199$ V. The potentials of conduction band minimum ($E_{\text{CBM(RHE)}}$) is further calculated as Eq. (2).

$$E_{\text{fb(RHE)}} = E_{\text{fb(Ag/AgCl)}} + E_{\text{AgCl}} + 0.059 \times \text{pH} \quad (1)$$

$$E_{\text{CBM(RHE)}} = E_{\text{fb(RHE)}} - 0.3 \quad (2)$$

2.5. Photocatalytic hydrogen production testing

Photocatalytic hydrogen evolution experiments were performed in buffer solution (pH = 7) under 300 W Xenon arc lamp irradiation (CEL-HXF300, CEAULight, China) with Pt as a co-catalyst and triethanolamine as a sacrificial reagent. The full-spectrum light intensity and visible light intensity measured were 204.5 mW/cm² and 104.2 mW/cm², respectively. The equipment employed for photocatalytic hydrogen evolution reaction was a gas-closed circulation system (CEL-SPH2N-D9, CEAULight, China) with a top-irradiation quartz vessel. For the photocatalytic hydrogen production, 18 mg of prepared photocatalysts was dispersed in the mixture solution containing 5 mL of triethanolamine, 45 mL of buffer solution, and 80 μ L of H₂PtCl₆ aqueous solution (10 mg/mL). The circulation system was kept in vacuum and the reaction vessel was sustained at 6 °C throughout measurement. The evolved hydrogen was collected and determined by a gas chromatography (GC-7920) at an interval of 0.5 h.

2.6. Computational method

The ground-state geometry optimization of the oligomers of TCPs was carried out using Gaussian 09 W program package with B3LYP hybrid functional and 6–31 G basis set. The total and partial DOS of the oligomers of TCPs as well as the molecular orbital composition analysis were obtained with Multiwfn analyzer (version 3.7). The electronic total energies of fragments of TCPs were computed by Gaussian 09 program package with additional single-point correction at B3LYP/6–31 G theory level. The average hydrogen adsorption free energies have been calculated through the Eq.(3):

$$\Delta G_{\text{H}} = G_{\text{fragment+H}} - G_{\text{fragment}} - (1/2)G_{\text{H}_2} \quad (3)$$

Where $G_{\text{fragment+H}}$, G_{fragment} , and G_{H_2} are the Gibbs free energies of the hydrogenated fragment, pristine fragment and hydrogen, respectively, with $G = U + PV - TS$. The vibrational, rotational and translational contributions (statistical mechanics contributions) were included in the calculation of internal energy (U) and entropy (S), i.e., $U = E_{\text{elect.}} + \text{ZPE} + U_{\text{vib}}^{\text{T}} + U_{\text{rot}} + U_{\text{trans}}$ where ZPE and $U_{\text{vib}}^{\text{T}}$ are the zero-point energy and vibrational contribution at finite temperature T, respectively. The Pt adsorption free energies were calculated by the similar program.

3. Results and discussion

3.1. Chemical structures of polymer catalysts

X-ray diffraction (XRD) patterns of the as-synthesized polymers clearly indicate their amorphous nature (Fig. S11). SEM images show the bulk morphology of TCP-2 and particle-like morphology of TCP-OXD

and TCP-BOXD (Fig. S12). The chemical structures of TCP-2, TCP-OXD, and TCP-BOXD were analyzed by ¹³C CP-MAS NMR spectroscopy and FT-IR spectroscopy. In ¹³C NMR spectra, the chemical shift around 170 ppm is the characteristic signal of carbon atoms in triazine heterocycles, and those located at the region of 142–126 ppm are ascribed to carbon atoms in phenylenes (Fig. 1). Weak signals of ~164 ppm and ~152 ppm appeared in TCP-OXD and TCP-BOXD are assigned to carbon atoms in 1,3,4-oxadiazole heterocycles (Fig. 1b, 1c). Moreover, typical FT-IR characteristic peaks of triazine heterocycle are clearly observed at 1510 cm⁻¹ and 1368 cm⁻¹ for TCP-2 (Fig. 1d), while these characteristic peaks can be confirmed at 1469 and 1318 cm⁻¹ by comparing TCP-OXD and TCP-BOXD with precursors (Figs. S13–S14).

Chemical environment of carbon, nitrogen and oxygen atoms in these samples were further analyzed by using XPS characterization (Fig. S15). The subpeaks of 284.8 eV and 286.3 eV deconvoluted from C1s spectra of all TCPs are associated with the phenylene and s-triazine buildings, respectively (Fig. 2a) [37]. While the peak of 287.4/287.8 eV only appeared in TCP-OXD and TCP-BOXD is assigned to the carbon atom in 1,3,4-oxadiazole heterocycle. Two N1s subpeaks of TCP-2 with binding energies of 398.7 and 400.3 eV originate from the C=N fragment in s-triazine heterocycle and pyrrolic nitrogen, respectively (Fig. 2b) [46–49]. However, the C=N in s-triazine heterocycle and C=N–N in 1,3,4-oxadiazole heterocycle are fitted at the binding energies of 398.2 eV and 399.6/399.8 eV, respectively, for TCP-OXD and TCP-BOXD [50]. TCP-BOXD has a relatively higher intensity ratio of peak 399.8 eV to peak 398.2 eV, due to the presence of more 1,3,4-oxadiazole heterocycles. For the O1s spectra (Fig. 2c), 532.1 eV and 534.1 eV peaks fitted in TCP-2 origin from adsorbed species, such as surface hydroxyls, water and CO₂ [51,52]. Compared with TCP-2, new O1s subpeak at binding energy of 531.1/531.3 eV found in TCP-OXD and TCP-BOXD can be assigned to the C–O–C in 1,3,4-oxadiazole heterocycle. All the above results imply the successful preparation of amorphous triazine-based conjugated skeleton polymers.

3.2. Band structure of polymer catalysts

The negative slope of Mott-Schottky plots of all TCPs indicates typical n-type semiconductor behavior (Fig. 3). The UV–visible diffuse reflectance spectra show that all the powder samples exhibit significant absorption in the ultraviolet region (Fig. S16), whereas TCPs containing 1,3,4-oxadiazole exhibits a red shifted absorption edge. Correspondingly, the optical band gaps are determined to be 2.97 eV, 2.41 eV and 2.85 eV, respectively, for TCP-2, TCP-OXD and TCP-BOXD (Fig. 3a). On the other hand, XPS valence band spectra reveal that valence band maximum (VBM) values of TCP-2, TCP-OXD and TCP-BOXD are 2.80, 2.45, and 2.71 eV (Fig. 3b), respectively. The recorded results can be further calibrated to 2.40, 2.05, and 2.31 eV (vs. RHE at pH = 0) because of the work function of XPS analyzer is ca. –0.4 eV (vs. RHE at pH = 0) [53,54]. Thereby, the energies of conduction band minimum (CBM) of TCP-2, TCP-OXD and TCP-BOXD are determined to be –0.57, –0.36 and –0.54 eV (Fig. 3c), which is basically consistent with results obtained from the Mott-Schottky analysis (Fig. 3d–f), which are more negative than the potential of H⁺/H₂ (0 V vs. RHE at pH = 0).

3.3. Hydrogen production performance and mechanism insights

Photocatalytic hydrogen evolution experiments were performed in buffer solution (pH = 7) under full-spectrum light irradiation with Pt and triethanolamine. As displayed in Fig. 4a, the hydrogen evolution in TCP-2 was very low throughout the illumination. However, when exposed to 4.5 h of light irradiation, TCP-OXD significantly increased its hydrogen production to 42 μ mol and TCP-BOXD to 189 μ mol. It is noteworthy that, despite the lower photocatalytic activity under visible light irradiation, TCP-OXD exhibited the highest visible-light driven H₂ evolution (Fig. S17), which is possibly due to its extended visible-light absorption (Fig. S16). In addition, negligible hydrogen production rate

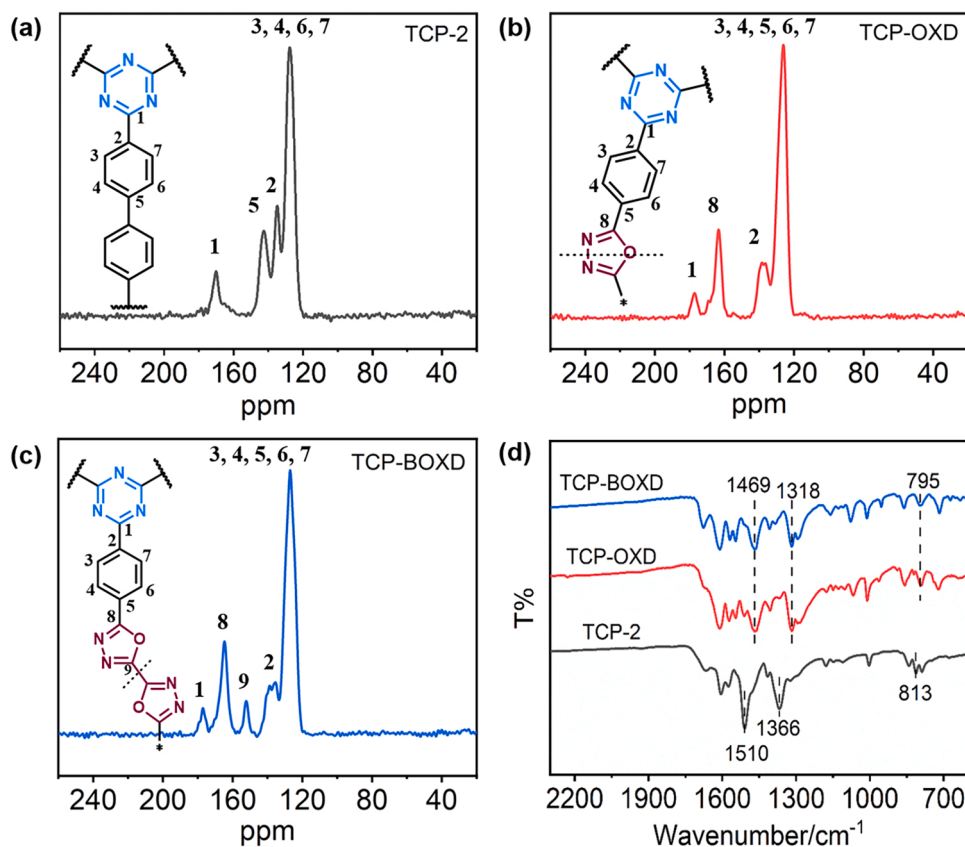


Fig. 1. Solid-state ^{13}C CP-MAS NMR spectra and FT-IR spectra of TCP-2, TCP-OXD and TCP-BOXD.

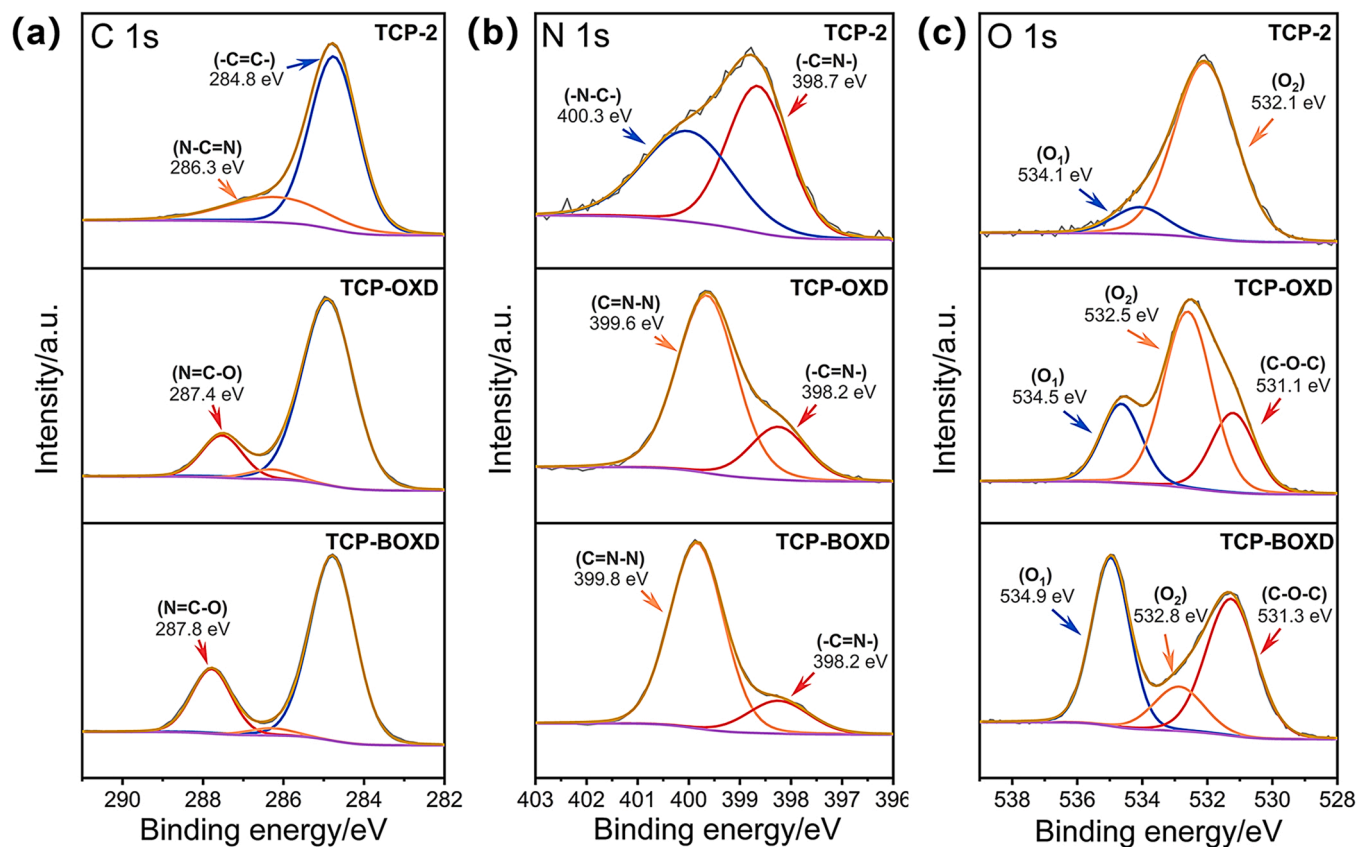


Fig. 2. The high-resolution XPS spectra of TCP-2, TCP-OXD and TCP-BOXD: (a) C 1s, (b) N 1s and (c) O 1s.

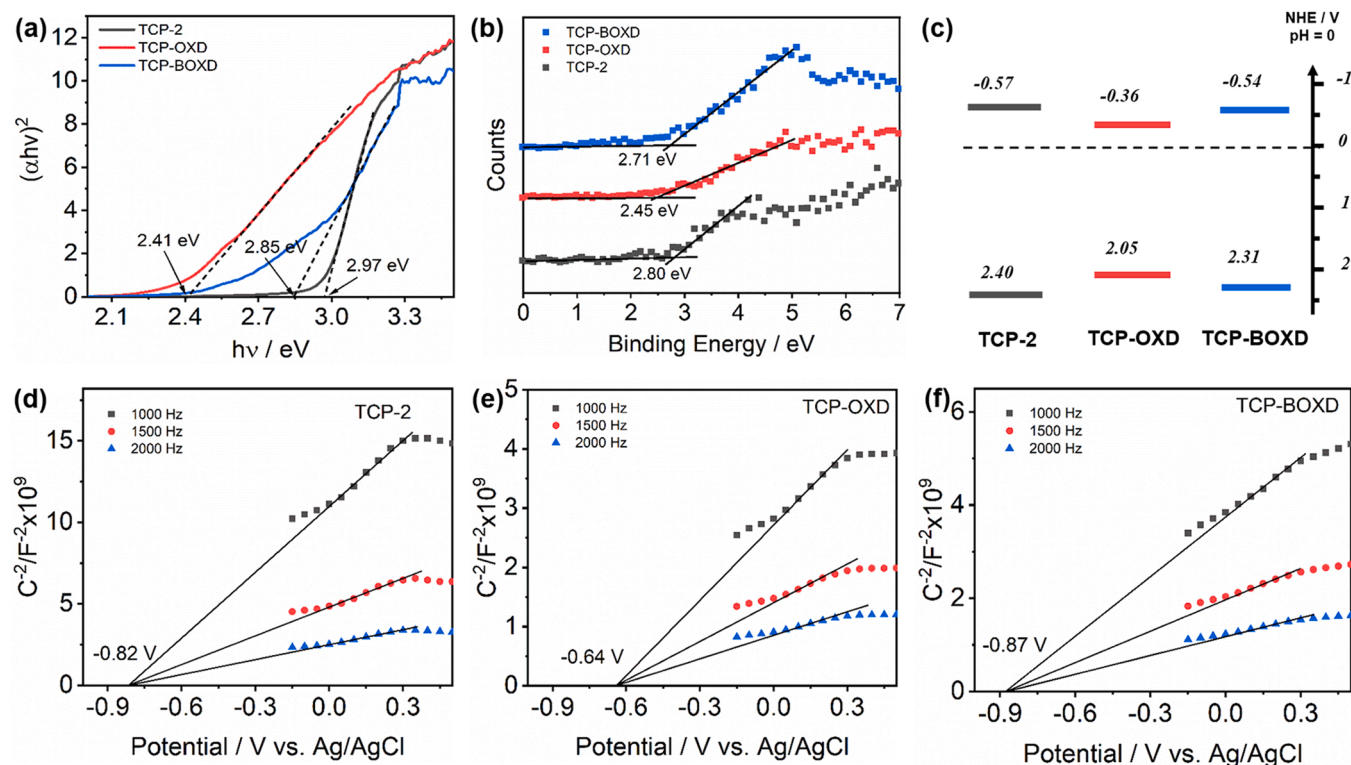


Fig. 3. (a) $(ah\nu)^2$ versus $h\nu$ plots, (b) valence band XPS spectra, and (c) band structure diagram and (d-f) Mott-Schottky plots of TCP-2, TCP-OXD and TCP-BOXD.

was monitored in the absence of Pt co-catalyst.

In order to uncover the photocatalytic enhancement of new TCPs (TCP-OXD, TCP-BOXD) under full-spectrum visible light irradiation, comparative study of their photophysical properties was conducted. All EPR spectra of the designed TCPs show a single Lorentzian paramagnetic absorption signal, where the g value is ca. 1.9999 closing to the free electron g value (2.0023). This phenomenon reveals electron delocalization in these TCPs (Fig. 4b). But the enhanced EPR signals of TCP-OXD and TCP-BOXD demonstrate more delocalization electrons [10]. Moreover, The transient state surface photovoltage (TS-SPV) spectra show a detectable positive signal, indicating photogenerated electrons migrated to the surface of TCPs under the built-in electric field (Fig. 4c) [55,56]. Remarkably, there are two obvious SPV response peaks in TCP-OXD and TCP-BOXD. Charge separation by drift under the built-in electric field is the main cause of the quick SPV response (R1 signal), whereas the charge separation and transportation by diffusion is the main cause of the slow SPV response (R2 signal) [57] TCP-BOXD exhibited a rather long carrier lifetime and stronger SPV signal, which demonstrates faster charge migration and more effective photogenerated charge separation. The conclusion can also be confirmed by the variation trend of photocurrent and electrochemical impedance results (Fig. 4d-e).

Charge carrier lifetime for as-synthesized TCP-2, TCP-OXD and TCP-BOXD was further investigated by transient absorption measurements. There are ground-state bleach (GSB) and photoinduced absorption (PIA) features observed for the three samples (Fig. S18). The GSB decays of TCP-2, TCP-OXD and TCP-BOXD can be well fitted by two components (Fig. 5a-c), a rapid lifetime of < 2 ps and a long lifetime of 0.4–3 ns, respectively. The rapid lifetime corresponds to the hole trapping from the VB band edges to certain band-gap trap states, while the long lifetime component reflects the exciton recombination (Fig. 5d) [58]. However, the long GSB decay lifetimes of TCP-2, TCP-OXD and TCP-BOXD are 402, 2907.4 and 1163.9 ps, respectively, reflecting their different trap depths. This deeper trap may hinder the detrapping of holes from the trap states and suppress the recombination between

excited electrons and holes, which explains why TCP-OXD and TCP-BOXD have more photogenerated electrons. In addition, the very slowly approaching of GSB decay plots to the $\Delta A = 0$ line features an extremely long lifetime, most likely suggesting another trap state possessing a rather deep depth [59]. For PIA decay dynamics, a short lifetime (< 0.6 ps) can be fitted in TCP-2, TCP-OXD and TCP-BOXD, which corresponds to the cooling of hot electrons [60,61]. Comparing to TCP-BOXD, another PIA decay lifetime (21.6 ps) fitted in TCP-OXD indicates an electron trap states located within the bandgap of TCP-OXD (Fig. S19), which may result in less photogenerated electrons escaping to the surface. Additionally, with time aging, the positive PIA signals convert to the negative bleaching signals at longer times, which may result from the sub-band gap trap-state absorption [62].

ESR spectra were also employed in order to give an insight into the redox capacity of photogenerated charge. Both the hydroxyl ($\bullet\text{OH}$) and superoxide ($\bullet\text{O}_2$) radicals were clearly detected for all catalysts under light illumination (Fig. 5e-f). The results propose that the electrons enable the reduction of H^+ , since the CBMs of TCPs are greater than the redox potential of $\text{O}_2/\bullet\text{O}_2$ (-0.046 V vs NHE) and the VBMs of TCPs are more positive than the redox potential of $\text{OH}^+/\bullet\text{OH}$ (1.99 V vs NHE) or $\text{H}_2\text{O}/\bullet\text{OH}$ (2.27 V). The signals of DMPO- $\bullet\text{OH}$ and DMPO- $\bullet\text{O}_2$ adducts are particularly prominent in the TCP-BOXD system, which indicates that more separated charge carriers migrated to the surface of TCP-BOXD. Additionally, compared with TCP-2 system, DMPO- $\bullet\text{OH}$ signal in TCP-OXD system is much stronger, but DMPO- $\bullet\text{O}_2$ signal is only a slightly higher, implying less free electrons with enough reduction potential (> -0.046 V) generating on the surface of TCP-OXD which may result from the electron being trapped by trapping state.

3.4. Theoretical calculations and analysis

Subsequently, DFT calculations were performed with Gaussian 09 W software package and Gaussian 09 package at the B3LYP3/6–31 level to further unveil the influence of the 1,3,4-oxadiazole building block on the photophysical properties [63]. Multiwfn program was employed to

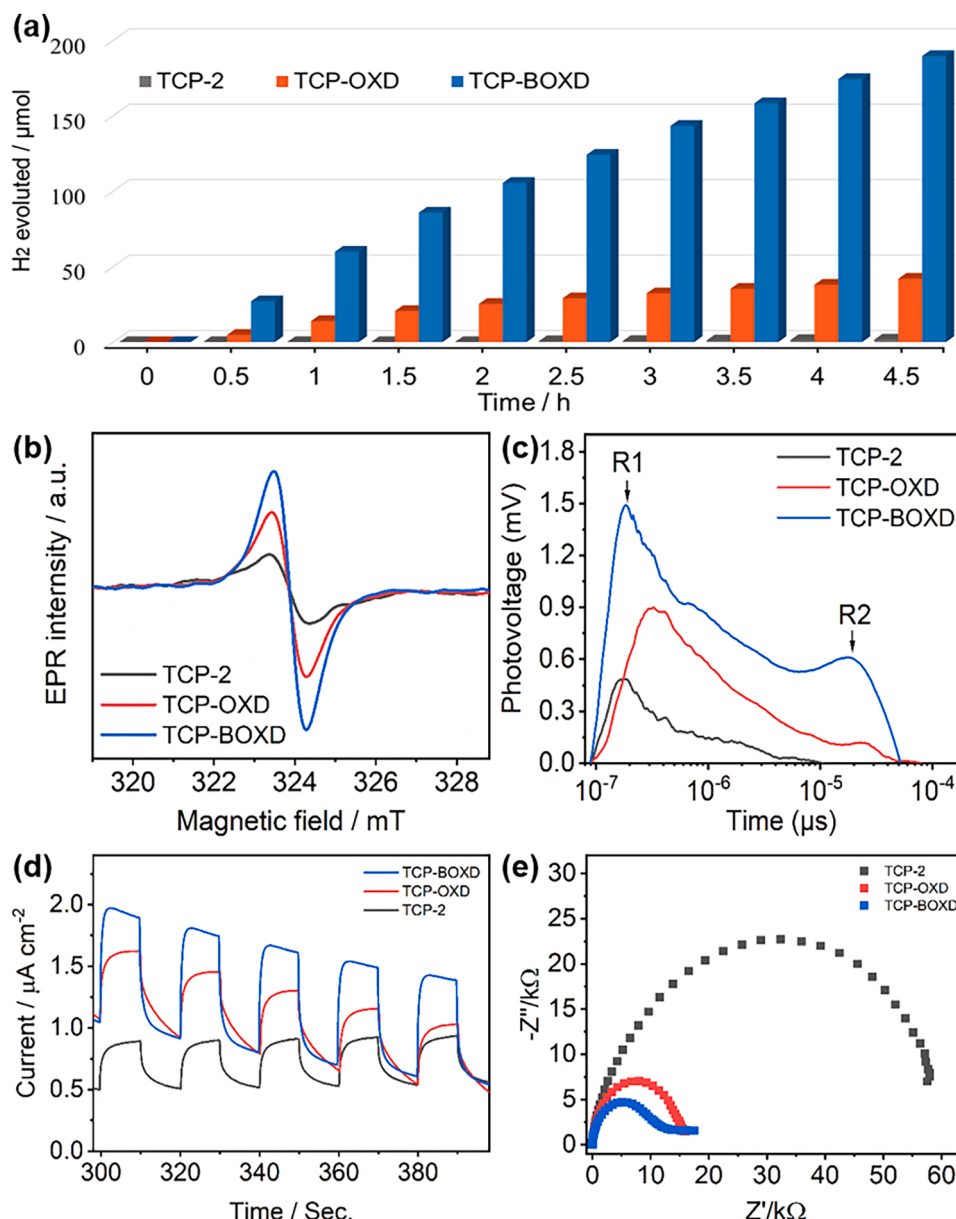


Fig. 4. (a) Photocatalytic H₂ evolution, (b) EPR spectra, (c) SPV signals, (d) photocurrent response curves, and (e) EIS Nyquist plots of TCP-2, TCP-OXD and TCP-BOXD under full arc light irradiation.

visualize the molecular orbital and density of states (DOS) [64]. The structural optimization results indicate that the diphenyl building blocks in the skeleton of TCP-2 is torsion with a dihedral angle (θ) of ca. 35° (Fig. S20). Following the 1,3,4-oxadiazole building block was implanted into the diphenyls, the obtained skeletons (TCP-OXD and TCP-BOXD) are almost coplanar (Figs. S21–S22), which further enhances the π -conjugation of polymer skeletons. This consequence is in accordance with the photoelectrochemical properties of TCPs. Furthermore, the calculated DOS curves of the oligomers are analyzed (Fig. S23). The energy around HOMO of TCP-2 oligomer has a mixed characteristic with a major contribution of diphenyl building blocks (Fig. 6a), suggesting the HOMO localized over the diphenyl moieties. Whereas, the energy around LUMO has the almost equal contribution of *s*-triazine and diphenyl building blocks, indicating that LUMO is delocalized over the skeleton. Therefore, the triazine and diphenyl units act as electron acceptor and donor, respectively [65]. On the other hand, P-OXD and P-BOXD constructed by the connection of tribenzyl-benzene to 1,3,4-oxadiazole and bi-1,3,4-oxadiazole, respectively, are also analyzed. 1,

3,4-oxadiazole and bi-1,3,4-oxadiazole are the major contributors to the LUMO states of P-OXD and P-BOXD oligomers (Figs. S24–S25), respectively, indicating their electron-drawing characteristic. Moreover, the higher contribution of bi-1,3,4-oxadiazole to LUMO states suggests much stronger electron pulling. However, when 1,3,4-oxadiazole or bi-1,3,4-oxadiazole is inserted into the skeleton of TCP-2 to form TCP-OXD and TCP-BOXD, the contribution of 1,3,4-oxadiazole and bi-1,3,4-oxadiazole to the HOMO and LUMO states is obvious as well (Fig. 6b, S26–S29), especially bi-1,3,4-oxadiazole shows almost equal contribution to the HOMO and LUMO states of TCP-BOXD oligomer. This phenomenon implies that 1,3,4-oxadiazole and bi-1,3,4-oxadiazole units act as π -bridges in TCP-OXD and TCP-BOXD to enhance the delocalized nature of HOMO and LUMO states. Based on above calculation results, some crucial conclusions can be drawn that *s*-triazine shows strong electron-drawing ability while bi-1,3,4-oxadiazole and 1,3,4-oxadiazole have much weaker. Moreover, when bi-1,3,4-oxadiazole or 1,3,4-oxadiazole is present in the *s*-triazine-based skeletons (TCP-OXD and TCP-BOXD), its electron-drawing nature will weaken the D-A interaction

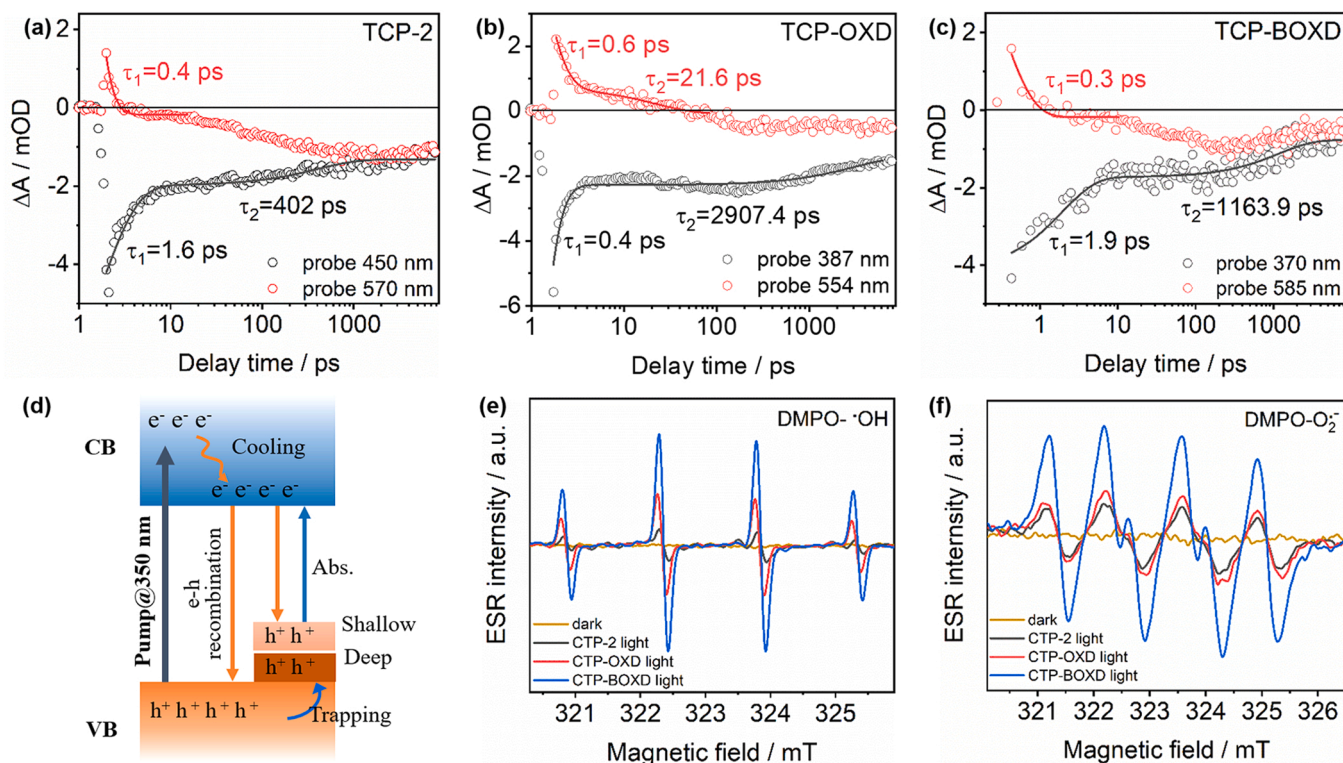


Fig. 5. PIA (top) and GSB (bottom) decay dynamics of (a) TCP-2 (b) TCP-OXD and (c) TCP-BOXD with the excitation of 350 nm pump pulse; (d) charge carrier dynamics models; (e, f) ESR spectra of catalysts under illumination in the presence of DMPO.

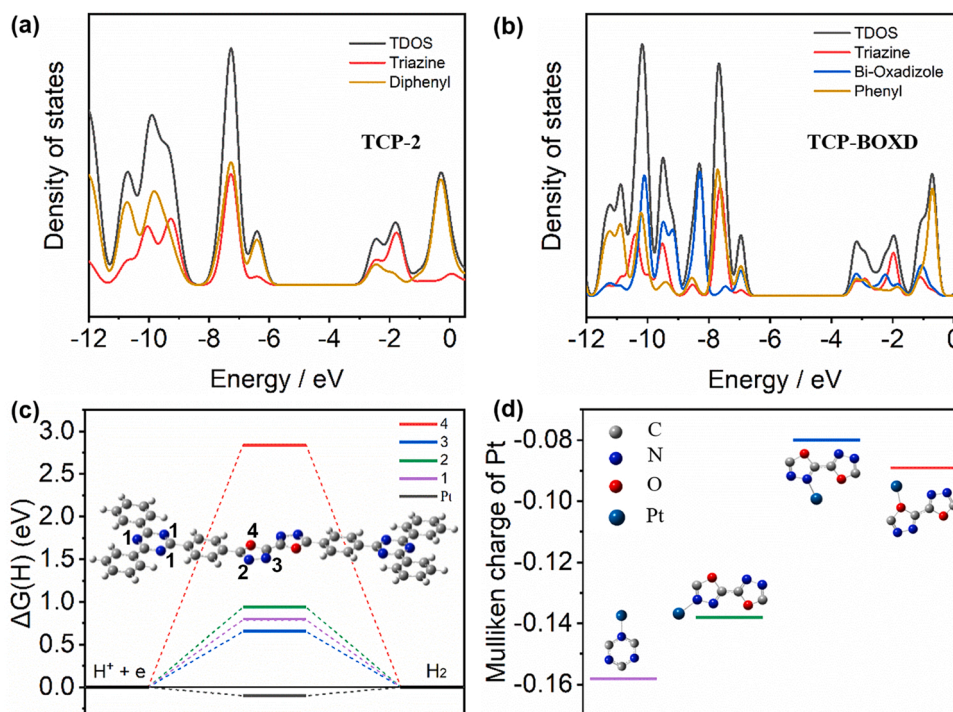


Fig. 6. Total and partial DOS for (a) TCP-2 and (b) TCP-BOXD oligomers; (c) Hydrogen adsorption free energy (ΔG_{H}) at the heteroatoms and (d) Mulliken atomic charges of platinum atom absorbed at the heteroatom sites.

between s-triazine and phenylene units. Thus, 1,3,4-oxadizole and bi-1,3,4-oxadizole can be deemed as π -bridges in TCP-OXD and TCP-BOXD for broadening the photoabsorption regions. In addition, the relatively stronger electron pulling of bi-1,3,4-oxadizole leads to a narrow

photoabsorption region for TCP-BOXD compared to TCP-OXD (Fig. S16).

On the other hand, the heteroatoms, such as N, S and O atoms, in the conjugated skeletons usually serve as active sites [66]. The adsorption

free energies (ΔG_H) of a single H atom adsorbing on the heteroatom sites were calculated (Fig. 6c), due to that the heteroatoms in the fragment of TCP-BOXD exhibit a higher electron density (Fig. S30). The ΔG_H at oxygen site in 1,3,4-oxadiazole unit is as high as 2.84 eV, while the ΔG_H at nitrogen sites in both *s*-triazine and 1,3,4-oxadiazole units are less than 1 eV, of which the lowest value of ΔG_H is 0.65 eV. Similar calculation results were obtained in the fragment of TCP-OXD (Fig. S31). These results indicate that the incorporation of 1,3,4-oxadiazole unit may increase the adsorbed sites of H atom, but the thermodynamics of the H^+/H_2 reaction still cannot be satisfied, which can expound no H_2 evolving in absent of Pt. Whereafter, Mulliken atomic charge values of Pt absorbed at the heteroatoms were further calculated (Fig. 6d), which can fully reflect the interactions between Pt and heteroatoms. The negative Mulliken atomic charge values obtained indicate that all heteroatoms output electrons to Pt, which can facilitate the H^+/H_2 reaction. In detail, Pt at the N sites in *s*-triazine has a most negative Mulliken atomic value (−0.158), and Pt at the N site “2” in 1,3,4-oxadiazole unit show a value of −0.138, which indicates that the introduction of 1,3,4-oxadiazole into skeletons increases the photocatalytic active sites.

4. Conclusions

In summary, for the first time, 1,3,4-oxadiazole unit was successfully introduced into the triazine-based skeleton to construct new π -conjugated polymers. The findings of this work verify that the electron-drawing nature of 1,3,4-oxadiazole not only broadens the light absorption band, but also promotes the separation and migration of photogenerated charge carriers. More interestingly, the N atoms in 1,3,4-oxadiazole, together with their counterparts in the triazine ring, have proved to be synergistic bi-active sites for the enhanced photocatalytic hydrogen evolution. TAS results indicate the trap states within bandgaps captured the photogenerated charge carriers to suppress the electron-hole recombination.

CRediT authorship contribution statement

Zhaolin Li: Investigation, Data curation, Formal analysis, Writing – original draft. **Hua Fang:** Software, Resources, Methodology. **Zupeng Chen:** Data curation, Writing – review & editing. **Weixin Zou:** Validation, Formal analysis. **Chengxiao Zhao:** Supervision, Project administration, Funding acquisition. **Xiaofei Yang:** Conceptualization, Supervision, Writing – review & editing, Funding acquisition.

Declaration of Competing Interest

The authors declare that they have no known competing financial interests or personal relationships that could have appeared to influence the work reported in this paper.

Acknowledgements

This work was financially supported by the National Natural Science Foundation of China (22005149, 21975129), Natural Science Foundation of Jiangsu Province (BK20200777), Natural Science Foundation of the Higher Education Institutions of Jiangsu Province, China (20KJB430034) and Science Fund for Distinguished Young Scholars (JC2019002), Nanjing Forestry University.

Appendix A. Supporting information

Supplementary data associated with this article can be found in the online version at [doi:10.1016/j.apcatb.2022.121374](https://doi.org/10.1016/j.apcatb.2022.121374).

References

- [1] Y. Feng, M. Xu, H. Liu, W. Li, H. Li, Z. Bian, Charge separation and interfacial selectivity induced by synergistic effect of ferroelectricity and piezoelectricity on $PbTiO_3$ monocrystalline nanoplates, *Nano Energy* 73 (2020), 104768, <https://doi.org/10.1016/j.nanoen.2020.104768>.
- [2] Y. Chen, Q. Qiao, J. Cao, H. Li, Z. Bian, Precious metal recovery, *Joule* 5 (2021) 3097–3115, <https://doi.org/10.1016/j.joule.2021.11.002>.
- [3] P. Lyu, J. Zhu, C. Han, L. Qiang, L. Zhang, B. Mei, J. He, X. Liu, Z. Bian, H. Li, Self-driven reactive oxygen species generation via interfacial oxygen vacancies on carbon-coated TiO_{2-x} with versatile applications, *ACS Appl. Mater. Interfaces* 13 (2021) 2033–2043, <https://doi.org/10.1021/acsami.0c19414>.
- [4] H. Liu, Y. Feng, J. Shao, Y. Chen, Z.L. Wang, H. Li, X. Chen, Z. Bian, Self-cleaning triboelectric triboenergy generator based on TiO_2 photocatalysis, *Nano Energy* 70 (2020), 104499, <https://doi.org/10.1016/j.nanoen.2020.104499>.
- [5] X. Deng, Y. Chen, J. Wen, Y. Xu, J. Zhu, Z. Bian, Polyaniline- TiO_2 composite photocatalysts for light-driven hexavalent chromium ions reduction, *Sci. Bull.* 65 (2020) 105–112, <https://doi.org/10.1016/j.scib.2019.10.020>.
- [6] Y. Chen, M. Xu, J. Wen, Y. Wan, Q. Zhao, X. Cao, Y. Ding, Z.L. Wang, H. Li, Z. Bian, Selective recovery of precious metals through photocatalysis, *Nat. Sustain.* 4 (2021) 618–626, <https://doi.org/10.1038/s41893-021-00697-4>.
- [7] H. Che, X. Gao, J. Chen, J. Hou, Y. Ao, P. Wang, Iodide-induced fragmentation of polymerized hydrophilic carbon nitride for high-performance quasi-homogeneous photocatalytic H_2O_2 production, *Angew. Chem. Int. Ed.* 60 (2021) 25546–25550, <https://doi.org/10.1002/anie.202111769>.
- [8] Q. Liu, J. Hou, J. Wu, L. Miao, G. You, Y. Ao, Intimately coupled photocatalysis and biodegradation for effective simultaneous removal of sulfamethoxazole and COD from synthetic domestic wastewater, *J. Hazard. Mater.* 423 (2022), 127063, <https://doi.org/10.1016/j.jhazmat.2021.127063>.
- [9] S. Zhou, Y. Wang, K. Zhou, D. Ba, Y. Ao, P. Wang, In-situ construction of Z-scheme $g-C_3N_4/VO_2$ composite with enhanced visible-light responsive performance for nitenpyram degradation, *Chin. Chem. Lett.* 32 (2021) 2179–2182, <https://doi.org/10.1016/j.cclet.2020.12.002>.
- [10] Y. Lu, X. Cui, C. Zhao, X. Yang, Highly efficient tandem Z-scheme heterojunctions for visible light-based photocatalytic oxygen evolution reaction, *Water Sci. Eng.* 13 (2020) 299–306, <https://doi.org/10.1016/j.wse.2020.12.005>.
- [11] F. Chen, H.F. Feng, W. Luo, P. Wang, H.G. Yu, J.J. Fan, Simultaneous realization of direct photodeposition and high H_2 -production activity of amorphous cobalt sulfide nanodot-modified rGO/TiO_2 photocatalyst, *Rare Met.* 40 (2021) 3125–3134, <https://doi.org/10.1007/s12598-021-01755-8>.
- [12] W.W. Liu, J. Pan, R.F. Peng, Shape-dependent hydrogen generation performance of PtPd bimetallic co-catalyst coupled with C_3N_4 photocatalyst, *Rare Met.* 40 (2021) 3554–3560, <https://doi.org/10.1007/s12598-021-01705-4>.
- [13] S. Zulfiqar, S. Liu, N. Rahman, H. Tang, S. Shah, X.H. Yu, Q.Q. Liu, Construction of S-scheme MnO_2/CdS heterojunction with core-shell structure as H_2 -production photocatalyst, *Rare Met.* 40 (2021) 2381–2391, <https://doi.org/10.1007/s12598-020-01616-w>.
- [14] B. He, M. Feng, X. Chen, J. Sun, Multidimensional (0D–3D) functional nanocarbon: promising material to strengthen the photocatalytic activity of graphitic carbon nitride, *Green Energy Environ.* 6 (2021) 823–845, <https://doi.org/10.1016/j.gee.2020.07.011>.
- [15] M. Zubair, E.M.M. Vanhaecke, I.H. Svernum, M. Rønning, J. Yang, Core-shell particles of C-doped CdS and graphene: a noble metal-free approach for efficient photocatalytic H_2 generation, *Green Energy Environ.* 5 (2020) 461–472, <https://doi.org/10.1016/j.gee.2020.10.017>.
- [16] S. Yanagida, A. Kabumoto, K. Mizumoto, K.Y.C. Pac, Poly(p-phenylene)-catalysed photoreduction of water to hydrogen, *J. Chem. Soc., Chem. Commun.* (1985) 474–475, <https://doi.org/10.1039/C3985000044>.
- [17] C.X. Zhao, Z.P. Chen, R. Shi, X.F. Yang, T.R. Zhang, Recent advances in conjugated polymers for visible-light-driven water splitting, *Adv. Mater.* 32 (2020), 1907296, <https://doi.org/10.1002/adma.201907296>.
- [18] Q. Yang, M.L. Luo, K.W. Liu, H.M. Cao, H.J. Yan, Covalent organic frameworks for photocatalytic applications, *Appl. Catal. B Environ.* 276 (2020), 119174, <https://doi.org/10.1016/j.apcatb.2020.119174>.
- [19] R.S. Sprick, J.X. Jiang, B. Bonillo, S.J. Ren, T. Ratvijitvech, P. Guiglion, M. A. Zwiñenburg, D.J. Adams, A.I. Cooper, Tunable organic photocatalysts for visible-light-driven hydrogen evolution, *J. Am. Chem. Soc.* 137 (2015) 3265–3270, <https://doi.org/10.1021/ja511552k>.
- [20] L. Stegbauer, S. Zech, G. Savasci, T. Banerjee, F. Podjaski, K. Schwinghammer, C. Ochsenfeld, B.V. Lotsch, Tailor-made photoconductive pyrene-based covalent organic frameworks for visible-light driven hydrogen generation, *Adv. Energy Mater.* 8 (2018), 1703278, <https://doi.org/10.1002/aenm.201703278>.
- [21] X.Y. Yan, D.H. Li, L.X. Zhang, X.J. Long, D.J. Yang, Tuning oxygen-containing groups of pyrene for high hydrogen peroxide production selectivity, *Appl. Catal. B Environ.* 304 (2022), 120908, <https://doi.org/10.1016/j.apcatb.2021.120908>.
- [22] P. Guiglion, C. Butchosa, M.A. Zwiñenburg, Polymeric watersplitting photocatalysts: a computational perspective on the water oxidation conundrum, *J. Mater. Chem. A* 2 (2014) 11996–12004, <https://doi.org/10.1039/C4TA02044H>.
- [23] W.L. Li, Z. Wei, K.J. Zhu, W.Q. Wei, J. Yang, J.F. Jing, D.L. Phillips, Y.F. Zhu, Nitrogen-defect induced trap states steering electron-hole migration in graphite carbon nitride, *Appl. Catal. B Environ.* (2022), 121142, <https://doi.org/10.1016/j.apcatb.2022.121142>.
- [24] Y.P. Hu, W. Huang, H.S. Wang, Q. He, Y. Zhou, P. Yang, Y.Y. Li, Y.G. Li, Metal-free photocatalytic hydrogenation using covalent triazine polymers, *Angew. Chem. Int. Ed.* 59 (2020) 14378–14382, <https://doi.org/10.1002/anie.202006618>.

- [25] L.P. Guo, Y.L. Niu, S. Razzaque, B. Tan, S.B. Jin, Design of D-A₁-A₂ covalent triazine frameworks via copolymerization for photocatalytic hydrogen evolution, *ACS Catal.* 9 (2019) 9438–9445, <https://doi.org/10.1021/acscatal.9b01951>.
- [26] M.Q. Liu, L.P. Guo, S.B. Jin, B.E. Tan, Covalent triazine frameworks: synthesis and applications, *J. Mater. Chem. A* 7 (2019) 5153–5172, <https://doi.org/10.1039/c8ta12442f>.
- [27] Z.F. Qian, Z.J. Wang, K.A.I. Zhang, Covalent triazine frameworks as emerging heterogeneous photocatalysts, *Chem. Mater.* 33 (2021) 1909–1926, <https://doi.org/10.1021/acs.chemmater.0c04348>.
- [28] Y.L. Yang, H.Y. Niu, L. Xu, H. Zhang, Y.Q. Cai, Triazine functionalized fully conjugated covalent organic framework for efficient photocatalysis, *Appl. Catal. B Environ.* 269 (2020), 118799, <https://doi.org/10.1016/j.apcatb.2020.118799>.
- [29] S.Q. Zhang, G. Cheng, L.P. Guo, N. Wang, B.E. Tan, S.B. Jin, Strong-base-assisted synthesis of a crystalline covalent triazine framework with high hydrophilicity via benzylamine monomer for photocatalytic water splitting, *Angew. Chem. Int. Ed.* 59 (2020) 6007–6014, <https://doi.org/10.1002/anie.201914424>.
- [30] J.J. Xie, S.A. Shevlin, Q.S. Ruan, S.J.A. Moniz, Y.R. Liu, X. Liu, Y.M. Li, C.C. Lau, Z. X. Guo, J.W. Tang, Efficient visible light-driven water oxidation and proton reduction by an ordered covalent triazine-based framework, *Energy Environ. Sci.* 11 (2018) 1617–1624, <https://doi.org/10.1039/C7EE02981K>.
- [31] H. Wang, H. Wang, Z.W. Wang, L. Tang, G.M. Zeng, P. Xu, M. Chen, T. Xiong, C. Y. Zhou, X.Y. Li, D.N. Huang, Y. Zhu, Z.X. Wang, J.W. Tang, Covalent organic framework photocatalysts: structures and applications, *Chem. Soc. Rev.* 49 (2020) 4135–4165, <https://doi.org/10.1039/D0CS00278J>.
- [32] W. Huang, Q. He, Y.P. Hu, Y.G. Li, Molecular heterostructures of covalent triazine frameworks for enhanced photocatalytic hydrogen production, *Angew. Chem. Int. Ed.* 58 (2019) 8676–8680, <https://doi.org/10.1002/anie.201900046>.
- [33] D. Schwarz, A. Acharja, A. Ichangi, P. Lyu, M.V. Opanasenko, F.R. Gossler, T.A. F. Konig, J. Cejka, P. Nachtigall, A. Thomas, M.J. Bojdys, Fluorescent sulphur- and nitrogen-containing porous polymers with tuneable donor-acceptor domains for light-driven hydrogen evolution, *Chem.-Eur. J.* 24 (2018) 11916–11921, <https://doi.org/10.1002/chem.201802902>.
- [34] G.B. Wang, S. Li, C.X. Yan, Q.Q. Lin, F.C. Zhu, Y. Geng, Y.B. Dong, A benzothiadiazole-based covalent organic framework for highly efficient visible-light driven hydrogen evolution, *Chem. Commun.* 56 (2020) 12612–12615, <https://doi.org/10.1039/D0CC00522A>.
- [35] J. Han, Z.B. Zhu, N.J. Li, D.Y. Chen, Q.F. Xu, H. Li, J.H. He, J.M. Lu, Metalloporphyrin-based D-A type conjugated organic polymer nanotube for efficient photocatalytic degradation, *Appl. Catal. B Environ.* 291 (2021), 120108, <https://doi.org/10.1016/j.apcatb.2021.120108>.
- [36] Y.Y. Wan, L. Wang, H.X. Xu, X.J. Wu, J.L. Yang, A simple molecular design strategy for two-dimensional covalent organic framework capable of visible-light-driven water splitting, *J. Am. Chem. Soc.* 142 (2020) 4508–4516, <https://doi.org/10.1021/jacs.0c00564>.
- [37] L. Chen, L. Wang, Y.Y. Wan, Y. Zhang, Z.M. Qi, X.J. Wu, H.X. Xu, Acetylene and diacetylene functionalized covalent triazine frameworks as metal-free photocatalysts for hydrogen peroxide production: a new two-electron water oxidation pathway, *Adv. Mater.* 32 (2020), 1904433, <https://doi.org/10.1002/adma.201904433>.
- [38] X.W. Lan, X.P. Liu, Y.Z. Zhang, Q. Li, J. Wang, Q.F. Zhang, G.Y. Bai, Unveiling charge dynamics in acetylene-bridged donor-pi-acceptor covalent triazine framework for enhanced photoredox catalysis, *ACS Catal.* 11 (2021) 7429–7441, <https://doi.org/10.1021/acscatal.1c01794>.
- [39] Y.S. Kochergin, D. Schwarz, A. Acharja, A. Ichangi, R. Kulkarni, P. Eliasova, J. Vacek, J. Schmidt, A. Thomas, M.J. Bojdys, Exploring the "Goldilocks Zone" of semiconducting polymer photocatalysts by donor-acceptor interactions, *Angew. Chem. Int. Ed.* 57 (2018) 14188–14192, <https://doi.org/10.1002/anie.201809702>.
- [40] U. Salzner, Does the donor-acceptor concept work for designing synthetic metals? 1. Theoretical investigation of poly(3-cyano-3'-hydroxybithiophene), *J. Phys. Chem. B* 106 (2002) 9214–9220, <https://doi.org/10.1021/jp020141i>.
- [41] R. Sun, B. Tan, Covalent triazine frameworks(CTFs) for photocatalytic applications, *Chem. Res. Chin. Univ.* (2022), <https://doi.org/10.1007/s40242-022-1468-4>.
- [42] F.Y. Chen, W.X. Zhang, T.J. Tian, B.L. Bai, H.T. Wang, M. Li, Substituent effect on intramolecular charge transfer of symmetric methoxy-substituted bi-1,3,4-oxadiazole derivatives, *J. Phys. Chem. A* 121 (2017) 8399–8407, <https://doi.org/10.1021/acs.jpca.7b08845>.
- [43] F.Y. Chen, W.X. Zhang, Z.J. Liu, L.Y. Meng, B.L. Bai, H.T. Wang, M. Li, Enhancement of intramolecular charge transfer strength in diphenylamine substituted symmetric 1,3,4-oxadiazole derivatives, *RSC Adv.* 9 (2019) 1–10, <https://doi.org/10.1039/C8RA08439D>.
- [44] C.X. Zhao, H.T. Wang, B.L. Bai, S.N. Qu, J.X. Song, X. Ran, Y. Zhang, M. Li, Organogels from unsymmetrical pi-conjugated 1,3,4-oxadiazole derivatives, *New J. Chem.* 37 (2013) 1454–1460, <https://doi.org/10.1039/c3nj40648b>.
- [45] J.H. Wang, T. Ding, K.F. Wu, Charge transfer from n-doped nanocrystals: mimicking intermediate events in multielectron photocatalysis, *J. Am. Chem. Soc.* 140 (2018) 7791–7794, <https://doi.org/10.1021/jacs.8b04263>.
- [46] J.S. Xu, C. Yang, S. Bi, W.Y. Wang, Y.F. He, D.Q. Wu, Q.F. Liang, X.C. Wang, F. Zhang, Vinylene-linked covalent organic frameworks (COFs) with symmetry-tuned polarity and photocatalytic activity, *Angew. Chem. Int. Ed.* 59 (2020) 23845–23853, <https://doi.org/10.1002/anie.202011852>.
- [47] Z. Xu, Y. Cui, B. Guo, H.Y. Li, H.X. Li, Boosting visible-light-driven H₂ evolution of covalent triazine framework from water by modifying Ni(II) pyrimidine-2-thiolate cocatalyst, *ChemCatChem* 13 (2021) 958–965, <https://doi.org/10.1002/cctc.202001631>.
- [48] K. Schwinghammer, S. Hug, M.B. Mesch, J. Senker, B.V. Lotsch, Phenyl-triazine oligomers for light-driven hydrogen evolution, *Energy Environ. Sci.* 8 (2015) 3345–3353, <https://doi.org/10.1039/c5ee02574e>.
- [49] Z.A. Lan, Y.X. Fang, Y.F. Zhang, X.C. Wang, Photocatalytic oxygen evolution from functional triazine-based polymers with tunable band structures, *Angew. Chem. Int. Ed.* 57 (2018) 470–474, <https://doi.org/10.1002/anie.201711155>.
- [50] W. Huang, J. Byun, I. Rorich, C. Ramanan, P.W.M. Blom, H. Lu, D. Wang, L.C. da Silva, R. Li, L. Wang, K. Landfester, K.A.I. Zhang, Asymmetric covalent triazine framework for enhanced visible-light photoredox catalysis via energy transfer cascade, *Angew. Chem. Int. Ed.* 57 (2018) 8316–8320, <https://doi.org/10.1002/anie.201801112>.
- [51] D. Goodacre, M. Blum, C. Buechner, H. Hoek, S.M. Gericke, V. Jovic, J.B. Franklin, S. Kittiwatanakul, T. Sohnell, H. Bluhm, K.E. Smith, Water adsorption on vanadium oxide thin films in ambient relative humidity, *J. Chem. Phys.* 152 (2020), 044715, <https://doi.org/10.1063/1.5138959>.
- [52] G. Pacholik, L. Enzlinger, A. Benzer, R. Rameshan, M. Latschka, C. Rameshan, K. Fottinger, In situ XPS studies of MoS₂-based CO₂ hydrogenation catalysts, *J. Phys. D Appl. Phys.* 54 (2021), 321002, <https://doi.org/10.1088/1361-6463/ac006f>.
- [53] D. Kong, X. Han, J. Xie, Q. Ruan, C.D. Windle, S. Gadipelli, K. Shen, Z. Bai, Z. Guo, J. Tang, Tunable covalent triazine-based frameworks (CTF-O) for visible-light-driven hydrogen and oxygen generation from water splitting, *ACS Catal.* 9 (2019) 7697–7707, <https://doi.org/10.1021/acscatal.9b02195>.
- [54] G. Greczynski, L. Hultman, X-ray photoelectron spectroscopy: towards reliable binding energy referencing, *Prog. Mater. Sci.* 107 (2020), 100591, <https://doi.org/10.1016/j.pmatsci.2019.100591>.
- [55] R.M. Doughty, F.A. Chowdhury, Z.T. Mi, F.E. Osterloh, Surface photovoltage spectroscopy observes junctions and carrier separation in gallium nitride nanowire arrays for overall water-splitting, *J. Chem. Phys.* 153 (2020), 144707, <https://doi.org/10.1063/5.0021273>.
- [56] K. Hu, Z.J. Li, L.L. Bai, F. Yang, X.Y. Chu, J. Bian, Z.Q. Zhang, H. Xu, L.Q. Jing, Synergetic subnano Ni- and Mn-oxo clusters anchored by chitosan oligomers on 2D g-C₃N₄ boost photocatalytic CO₂ reduction, *Sol. RRL* 5 (2020), 2000472, <https://doi.org/10.1002/solr.202000472>.
- [57] C.H. Kang, L.Q. Jing, T. Guo, H.C. Cui, J. Zhou, H.G. Fu, Mesoporous SiO₂-modified nanocrystalline TiO₂ with high anatase thermal stability and large surface area as efficient photocatalyst, *J. Phys. Chem. C* 113 (2009) 1006–1013, <https://doi.org/10.1021/jp807552u>.
- [58] Z.W. Chen, Q. Zhang, Y. Luo, Experimental identification of ultrafast reverse hole transfer at the interface of the photoexcited methanol/graphitic carbon nitride system, *Angew. Chem. Int. Ed.* 57 (2018) 5320–5324, <https://doi.org/10.1002/anie.201713102>.
- [59] H.Q. Xu, J.H. Hu, D.K. Wang, Z.H. Li, Q. Zhang, Y. Luo, S.H. Yu, H.L. Jiang, Visible-light photoreduction of CO₂ in a metal-organic framework: boosting electron-hole separation via electron trap states, *J. Am. Chem. Soc.* 137 (2015) 13440–13443, <https://doi.org/10.1021/jacs.5b08773>.
- [60] B. Yang, K.L. Han, Charge-carrier dynamics of lead-free halide perovskite nanocrystals, *Acc. Chem. Res.* 52 (2019) 3188–3198, <https://doi.org/10.1021/acs.accounts.9b00422>.
- [61] B. Yang, J.S. Chen, S.Q. Yang, F. Hong, L. Sun, P.G. Han, T. Pullerits, W.Q. Deng, K. L. Han, Lead-free silver-bismuth halide double perovskite nanocrystals, *Angew. Chem. Int. Ed.* 57 (2018) 5359–5363, <https://doi.org/10.1002/anie.201800660>.
- [62] B. Yang, X. Mao, F. Hong, W.W. Meng, Y.X. Tang, X.S. Xia, S.Q. Yang, W.Q. Deng, K.L. Han, Lead-free direct band gap double-perovskite nanocrystals with bright dual-color emission, *J. Am. Chem. Soc.* 140 (2018) 17001–17006, <https://doi.org/10.1021/jacs.8b07424>.
- [63] M.J. Frisch, G.W. Trucks, H.B. Schlegel, et al., Gaussian 09, Revision D.01, Gaussian, Inc., Wallingford CT (2009).
- [64] T. Lu, F.W. Chen, Multiwfn: A multifunctional wavefunction analyzer, *J. Comput. Chem.* 33 (5) (2012) 580–592, <https://doi.org/10.1002/jcc.22885>.
- [65] G. Damas, C.F.N. Marchiori, C.M. Araujo, On the design of donor acceptor conjugated polymers for photocatalytic hydrogen evolution reaction: first-principles theory-based assessment, *J. Phys. Chem. C* 122 (2018) 26876–26888, <https://doi.org/10.1021/acs.jpcc.8b09408>.
- [66] V.S. Vyas, F. Haase, L. Stegbauer, G. Savasci, F. Podjaski, C. Ochsenfeld, B. V. Lotsch, A tunable azine covalent organic framework platform for visible light-induced hydrogen generation, *Nat. Commun.* 6 (2015) 8508, <https://doi.org/10.1038/ncomms9508>.